Mapana – Journal of Sciences
2024, Vol. 23, No. 3, 81-102
ISSN 0975-3303 | https://doi.org/10.12723/mjs.70.5

Improved Photocatalytic and Bacterial Growth Inhibition Properties Realized for PbS/SnO_2-rGO Nanocomposite

C Rajashree*, AR Balu†, K Devendran‡, M Sriramraj§, V Rajamani** and N Arunkumar††

Abstract

PbS/SnO_2 (PS) and rGO-PbS/SnO_2 (rPS) nanocomposites (NCs) were synthesized through one-pot green synthesis and chemical precipitation methods. In this paper, a comparison of the synthesized composites' photodegradation and bacterial growth inhibition properties has been conducted. For both composites, XRD analyses show the presence of tetragonal-structured SnO_2 and cubic-structured PbS peaks. rGO blending increases PS crystallite size from 29 nm to 34 nm. rPS NC shows uniformly packed grains with well-defined boundaries. Absorption peaks of PS red shifts with rGO inclusion. The decreased band gap for rPS might be due to the synergistic effect of sulfur/oxygen vacancies and significant interaction between rGO and PbS/SnO_2 NC. The rPS catalyst demonstrated a maximum degradation efficiency of 93% against rhodamine B (*RhB*) dye. Antibacterial activity of PbS/SnO_2 improves with rGO inclusion. PS and rPS NCs are more resistant to gram-positive bacteria than gram-negative bacteria.

Keywords: Nanocomposite; reduced graphene oxide; heterojunction; bacterial resistance; zone of inhibition

* cmrajashree@gmail.com
† A Veeriya Vandayar Memorial Sri Pushpam College, Poondi; arbalu757@gmail.com
‡ devendran2187@gmail.com
§ Sriramrajphysics@gmail.com
** Sruthirithi14@gmail.com
†† aroon5465@gmail.com

1. Introduction

Semiconducting chalcogenides in nanoregime possess interesting physico-chemical properties. Lead sulfide (PbS), a strong quantization chalcogenide belonging to the IV-VI group, is characterized by a high dielectric constant and low electron and hole masses [1]. In addition to its excellent near infra-red (NIR) emitting properties, PbS exhibits third-order nonlinear optical properties and has a fast response time, so it is suitable for optical computing, display devices, real-time holography, optical correlation, solar control coatings, biological sensors, etc. [2]. PbS in the nano dimension finds applications as a photocatalyst and antimicrobial agent. The electrochemical properties of PbS are noteworthy [3]. However, many factors influence the physical properties of PbS, such as crystallinity, particle size, surface morphology, and so on. The aforementioned factors need to be changed in order to use PbS for a variety of applications. Doping or creating composites with other semiconductors are two ways to accomplish this. By coupling PbS with other semiconductors, charge carriers are transferred between them, potentially improving their physical properties [4].

Tin dioxide (SnO_2) is an excellent chemical and thermally stable semiconductor that is ideal for gas sensing, catalysis, and optoelectronic applications. It is a low-cost wide-band gap semiconductor (3.6 eV) [5]. Its many structural geometries and electronic structure make SnO_2 exhibit ferromagnetic behavior when doped with magnetic metal ions [6]. With the addition of impurity atoms, SnO_2 could be improved for dye-sensitized solar cells, gas sensors, and industrial and domestic applications by controlling oxygen vacancies [7]. PbS's band gap can be widened, and its thermal and chemical stability can be enhanced when SnO_2 is coupled, making it appropriate for optoelectronic, photocatalytic, electrochemical, and antimicrobial applications. Enhanced magnetic, catalytic, and antifungal characteristics of the PbS-SnO_2 nanocomposite were evidenced in our previous study [2]. Catalytic efficiency is frequently low due to the synthesized composite's rapid recombination rate and ineffective use of photogenerated electron-hole pairs [8]. Also, this composite has the tendency to coagulate, has poor dispersibility, and has the ability to form intermediate metal ion complexes, which limits its strong energy

storage ability, photodegradation efficiency, and microbial resistance potency. The limitations of the PbS/SnO_2 nanocomposite have been addressed in this work by utilizing reduced graphene oxide (rGO).

Graphene-based carbonaceous material rGO exhibits a single-layer 2D nanostructure formed by sp^2 hybridized carbon atoms, including hydroxyl, carboxyl, epoxy, etc [9]. Furthermore, they demonstrate greater surface area, high electron mobility, mechanical strength, and larger thermal conductivity [10]. In addition, rGO's hybridized network frames make it behave like a semiconductor. These qualities prove that the decoration of rGO with PbS/SnO_2 nanocomposite enables the development of a hybrid nanocomposite with outstanding properties, eliminating the demerits associated with PbS/SnO_2. rGO-PbS/SnO_2 nanocomposite has been synthesized by a one-pot synthesis method using aqueous phytoextract as a reductant prepared from *Psidium guajava* leaf, which contains plenty of flavonoids [11]. Flavonoids release hydrogen when their hydroxyl groups are activated, reducing GO to rGO [12]. As well as anchoring PbS/SnO_2 NPs to rGO sheets, the leaf extract also serves as a capping agent. Capping agents act as stabilizers that inhibit the over-growth of nanoparticles and prevent their aggregation/coagulation while synthesizing them. PbS/SnO_2 and rGO-PbS/SnO_2 nanocomposites were compared for their photocatalytic and antibacterial properties in this work. In literature, there exists plenty of rGO-incorporated sulfide/oxide-based nanocomposites synthesized for photocatalytic and antibacterial applications. A few of them are compiled in Table 1. With rGO blending, ZnO/NiO [13], ZnO/CdS [14], ZnO [15], CdS [16], NiO [17] and CuS [18] exhibited enhanced photocatalytic activities. Table 1 demonstrates the dearth of research on rGO-incorporated PbS or PbS-based composites, particularly those with photocatalytic and antibacterial qualities. Hence, this work will provide new insight for researchers working with rGO-blended PbS-based nanocomposites.

Compo-site	Synthesis method	Photocatalytic activity				Anti-bacterial activity against	Reference
		Dye	Light source	Irradia-tion time	Efficiency, η (%)		
ZnO/NiO -rGO	Wet chemical	MB	Solar light	120	89.72	---	[13]
ZnO/CdS -rGO	Hydro thermal	Cr(VI)	Visible	30	93.2	---	[14]
ZnO/rGO	One step	RhB	Visible	90	87	*E.coli*	[15]
CdS/rGO	Ultrasonic	MB	Visible	180	90.1	---	[16]
NiO-rGO	Thermal de-composition	MO	Sunlight	90	87	---	[17]
CuS-rGO	Co precipitation	MG	Sunlight	90	97.6	---	[18]

Table 1: Photocatalytic and antibacterial properties of rGO based nanocomposites in literature

2. Experimental studies

2.1 *Material used*

Graphene powder with 99 % purity was purchased from Adnano Technologies, India. Lead nitrate, thiourea, tin (II) chloride, and liquid NH_3 purchased from Sigma Aldrich, India, are used. RhB dye with 98% purity was supplied by Alpha Chemika, India. Mueller-Hinton (MH) agar was purchased from Himedia, India. Dimethyl sulfoxide (DMSO) was supplied from Meru Chem, India.

2.2 *Extraction of Psidium guajava* (*P. Guajava) leaf extract*

A mixture of water and ethanol (3:1) was used to wash and dry the leaves of *P. guajava*. The leaves, after being baked at 80ºC, were then crushed and ground into fine powder, of which 20 g was added to 30 min distilled water and maintained at 60°C for 30 min. After cooling and sedimenting at room temperature, the leaf extract was filtered.

2.3 *Synthesis of PS NC*

PbS and SnO_2 precipitates were obtained separately by dissolving 0.05 M lead nitrate and thiourea in one beaker and 0.1 M tin (II) chloride in another beaker in 140 mL water + 10 mL liquid NH_3. After stirring, the solutions were left undisturbed for 2 hours to produce PbS and SnO_2 precipitates. After collecting these precipitates, they

were mixed thoroughly, calcined for two hours at 250°C, and then crushed to obtain PS NC.

2.4 *Synthesis of rPS NC*

In 30 mL of water, 2 g of graphene oxide powder was dissolved and ultrasonically processed for 30 minutes. In 100 mL of water containing 0.1 M $SnCl_2$, 0.05 M lead nitrate, and thiourea, the GO dispersion was added and stirred for one hour. In this mixture, 20 mL of leaf extract, along with a few drops of NH_3 solution, was added to keep the pH at 9. The resultant solution was heated at 95° C for 4 hours and calcinated at 400°C for 2 h to obtain rPS NC.

2.5 *Characterization*

PS and rPS NCs were analyzed using a diffractometer (X-PERT PRO) with CuKα radiation (1.5406 Å). HITACHI S-3000H was used to characterize the morphology. UV-visible studies were done using a Perkin Elmer Lambda–25 Spectrophotometer. Using Perkin Elmer Rx-1, Fourier transform infrared (FT-IR) studies were conducted. Photoluminescence (PL) studies are done using a spectrophotometer (Varian Cary Eclipse).

2.6 *Photocatalytic experiment against RhB*

6 mg of PS and rPS catalysts were dispersed in 20 mL RhB solution. To obtain equilibrium adsorption and desorption of *RhB*, solutions were stirred in the dark for 20 minutes before exposure to visible light. Afterwards, the solutions were exposed to visible light (100 W incandescent lamp) with continuous stirring. A Perkin Elmer Lambda-25 spectrophotometer was used to analyze 4 mL of the reaction mixture every 20 minutes.

2.7 *Bacterial growth resistance*

Staphylococcus aureus (*S. aureus)* and *Escherichia coli* (*E. coli)* bacteria were cultured freshly in MH media. Assays were performed in 96-well plates with inoculums and 4 mg (optimized value, even though minimum inhibitory concentration being 1.5 mg) PS and rPS NCs dissolved in 50 µL DMSO. Following a 24-hour incubation period at 37°C, the inhibitory zones were tested for antibacterial activity.

3. Results and discussion

3.1 *XRD*

In PS and rPS, cubic structured PbS peaks were observed (Fig. 1) at 2θ equal to 26°, 30.05°, 43°, 50.9°, 53.4° and 71° which matched JCPDS No. 77-0244 [19].

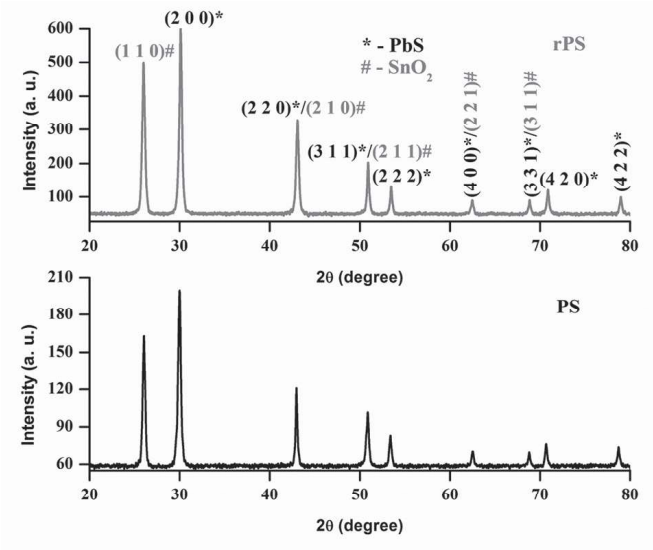

Fig.1 PS and rPS's XRD patterns

Tetragonal structured SnO_2 peaks were observed at 27.1°, 34.1°, 43°, 57.7°, indexed to (1 1 0), (1 0 1), (2 1 0) and (0 0 2) planes (JCPDS No. 88-0287) [20]. The dominant peaks were (2 0 0) for PbS and (1 1 0) for SnO_2. As evidenced by the shift in PbS and SnO2-related peaks towards higher 2θ values (Fig. 1) and an increase in the sharpness of the diffraction peaks, rGO's addition increases the degree of crystallinity of the PbS/SnO_2 NC [21]. The formation of a heterojunction between PbS and SnO_2 was confirmed by their related peaks. XRD patterns of rPS did not identify any peaks related to rGO, as lower amounts of graphene or fewer layers of rGO are present in the composite. The results show that GO has been successfully reduced to produce a rPS nanocomposite that contains only a few layers of rGO sheets [22]. The composites' crystallite size (D) was found using Scherrer's formula:

$$D = \frac{0.9}{\square\ \square\square\square} \qquad (1)$$

where β - full-width and half maximum of the peak and λ = 1.5406 x 10^{-10}m. The calculated sizes were 29 and 34 nm for PS and rPS composites.

3.2 *SEM*

PS and rPS NCs' SEM images are displayed in Fig. 2. For PS NC, tiny grains of various sizes are discernible.

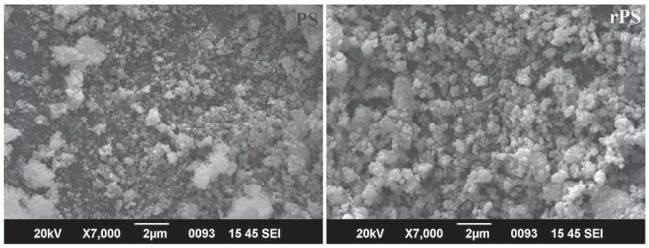

Fig.2 SEM images of PS and rPS

Grains appear clustered along with few empty sites. With rGO blending, rPS NC exhibited uniform distribution of tightly packed with well-defined boundaries. Grains size of PS got increased with rGO inclusion.

Pb, S, Sn, and O were confirmed to be present in both composites by EDS spectra (Fig. 3).

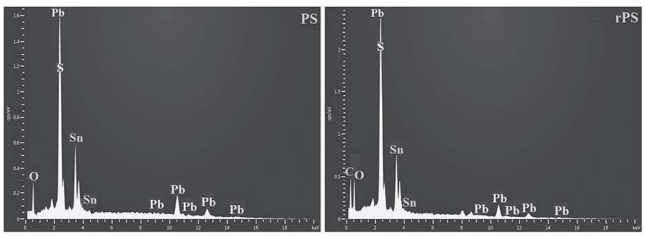

Fig.3 PS and rPS's EDS spectra

In the presence of these peaks, the heterojunction between PbS and SnO_2 was confirmed. rGO inclusion in rPS NC was ascertained from the presence of peak related to C. In PS and rPS NCs, Table 2 shows the atomic weight percentages of Pb, S, Sn, O, and C.

Nanocomposite	at. wt. %				
	Pb	S	Sn	O	C
PS	28.73	22.25	27.48	21.54	---
rPS	26.84	23.61	25.82	19.5	4.23

Table 2: Elemental composition of Pb, S, Sn, O and C in PS and rPS NCs

3.3 *Optical studies*

PS exhibits two absorption peaks at 645 and 348 nm corresponding to PbS and SnO_2 (Fig. 4(a)).

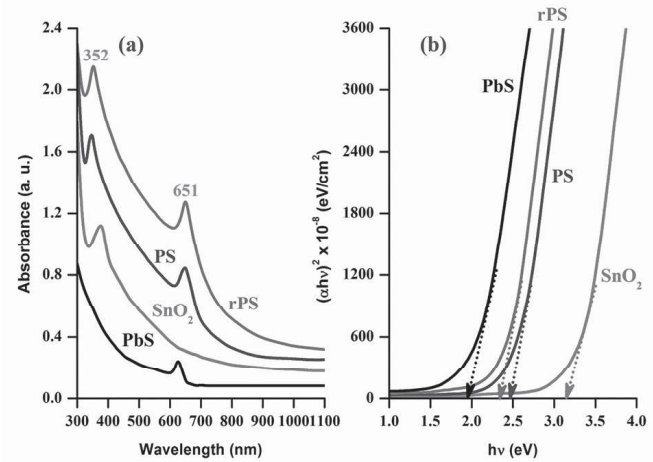

Fig.4 PbS, SnO_2, PS, and rPS's a) Absorbance spectra and b) Tauc plots

Due to bonding, as well as charge delocalization from electronic interaction between PbS/SnO_2 and rGO, the position of these peaks got red shifted [23, 24]. Moreover, because rGO can raise the surface electric charge of PbS/SnO_2, rPS shows continuous absorbance in the visible range [25]. The rPS composite is, therefore, more efficient at utilizing visible light and appears to perform better in terms of degradation. The red shifting of the absorption peaks of the rPS composite indicates a decrease in its band gap value and an increase in the size of PbS/SnO_2 NC with rGO inclusion. Thus, rGO acts as the supporter, helping the PbS/SnO_2 NPs to disperse and prevent them from aggregating [21]. The enhanced surface morphology observed for the rPS NC (Fig. 2) clearly supports this. The energy gaps between the values of PbS (1.96 eV) and SnO_2 (3.18 eV) were 2.48 and 2.36 eV for PS and rPS NCs (Fig. 4(b)). Sulfur/oxygen vacancies and significant interfacial interactions between rGO and PbS/SnO_2 NC could account for the decreased band gap for rPS [26].

3.4 *FTIR Studies*

FTIR spectra of PS and rPS nanocomposites (Fig. 5) show OH stretching vibrations (~ at 3418 cm^{-1}) due to interlayer water molecules [27].

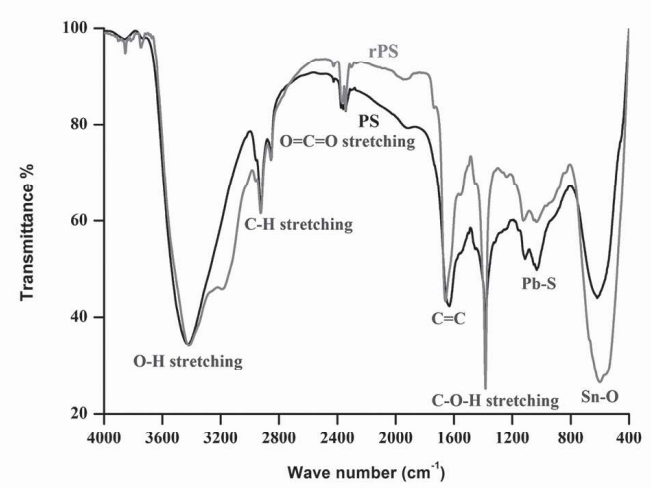

Fig.5 PS and rPS's FTIR spectra

The presence of amino group resulted in C=C stretching at 1385 cm^{-1} [28]. Pb–S related bands (1384 - 600 cm^{-1}) are caused by heteropolar lead sulfide molecules [1]. C–H stretchings observed around at 2925 cm^{-1} arise from alkyl groups. O=C=O symmetric stretching of carboxyl group occurs at 2366 [27]. SnO_2 band is seen at 599 cm^{-1} for both PS and rPS [29]. As PbS and SnO_2 form a composite, both PS and rPS show Pb-S and Sn-O bands. rPS peak intensity is significantly reduced when PbS/SnO_2 is attached to rGO sheets [30].

3.5 *PL studies*

PS and rPS NCs exhibit PL emission bands at 361, 375, 392, 410, 436, 459, 495, and 505 nm (Fig. 6). Recombination of free exciton is ascribed to the UV emission peaks at 361 and 375 nm [31]. Transitions of electrons from the localized level to the valence band produced a near band-edge emission (NBE) peak at 392 nm [32]. In PbS, at 410 nm, conduction band electrons give way to trapped holes at interstitial Pb^{2+} sites [33].

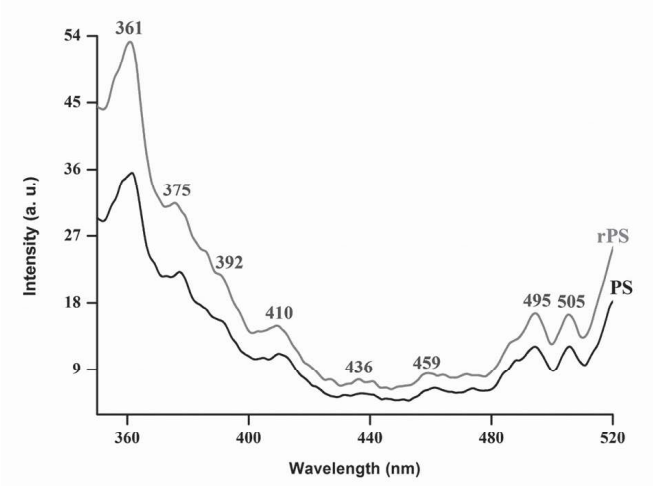

Fig.6 PS and rPS's PL spectra

An exciton attached to a donor peaks at 436 nm. Structure defects/ luminescent centers in SnO_2 emit the 459 nm peak [34]. The peak at 495 nm is associated with S vacancies present in both PS and rPS [35]. The donor-acceptor pair emits the 505 nm peak [36].

3.6 *Photocatalytic activity*

We tested PS and rPS NCs' photocatalytic activity against rhodamine B. Absorbance spectra taken at regular intervals of 20 min (Fig. 7) showed that the intensity decreases as irradiation time increases with the presence of PS and rPS catalysts, confirming the fact that the pollutant was degraded and the dye concentration got decreased. RhB decomposition happens for both PS and rPS with light irradiation (Fig. 8). The degradation efficiencies calculated using the relation,

$$\eta = \left(1 - \frac{C}{C_0}\right) \times 100\% \qquad (2)$$

(where C and C_0 are concentrations of dye under light and dark conditions) are displayed in Fig. 9. After 100 min, the calculated η values were 82.5 and 93 % for PS and rPS catalysts, respectively.

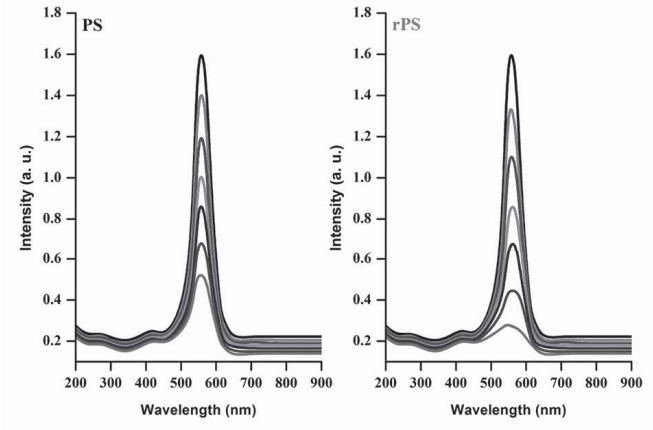

Fig.7 Absorbance spectra of PS and rPS catalysts

The anchoring of PbS/SnO_2 NC on rGO sheets resulted in improved degradation efficiency due to a high surface-to-volume ratio, increased active sites for dye adsorption, and a lower recombination rate of photogenerated species [37].

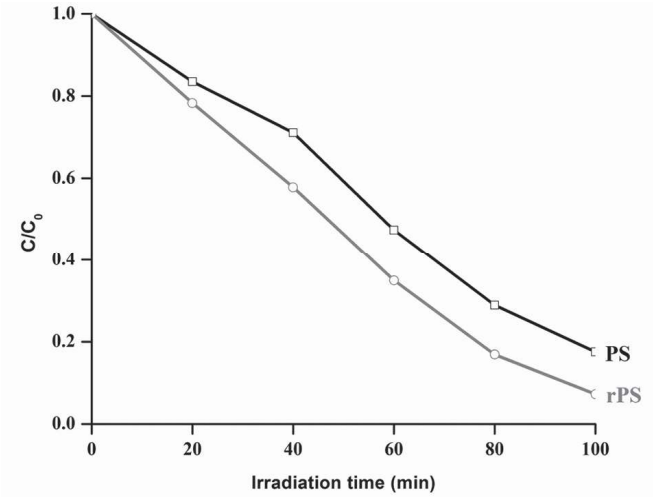

Fig.8 C/C_0 versus reaction time graphs of PS and rPS

The enhanced degradation efficiency of rPS is initiated by rGO blending, which has a tremendous amount of electrons causing more ROS (OH^*, O_2^{*-}) generation, thereby increasing the separation of electron-hole pairs [38]. Additionally, the rate of the degradation reaction is accelerated by the RhB dye molecules adsorbed on the surface of rPS through the primary atomic force field and π-π interactions of rGO.

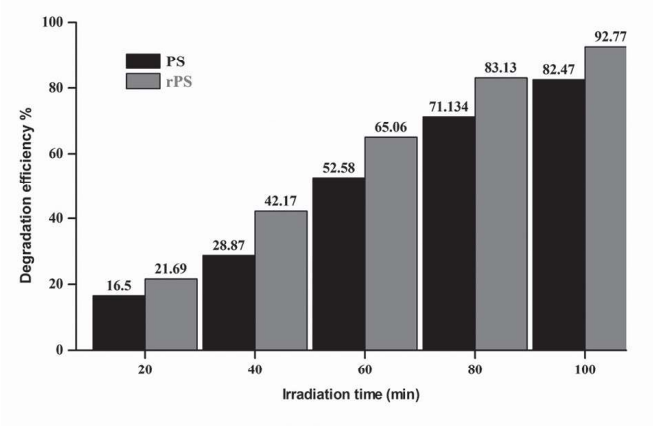

Fig.9 PS and rPS's degradation efficiencies

The first order kinetics (Langmuir-Hinshelwood model) involved obeys the relation:

$$ln\left(\frac{C_0}{C}\right) = kt \qquad (3)$$

where k, $C_{0,}$ and C are rate constant concentrations of RhB under dark and after time 't'. From Fig. 10, the k values of PS (0.0189 min^{-1}) and rPS (0.0265 min^{-1}) are determined from their slopes. The high value of k demonstrated the tremendous photocatalytic activity of rPS NC due to the formation of heterojunction between rGO and PbS/SnO_2 NC.

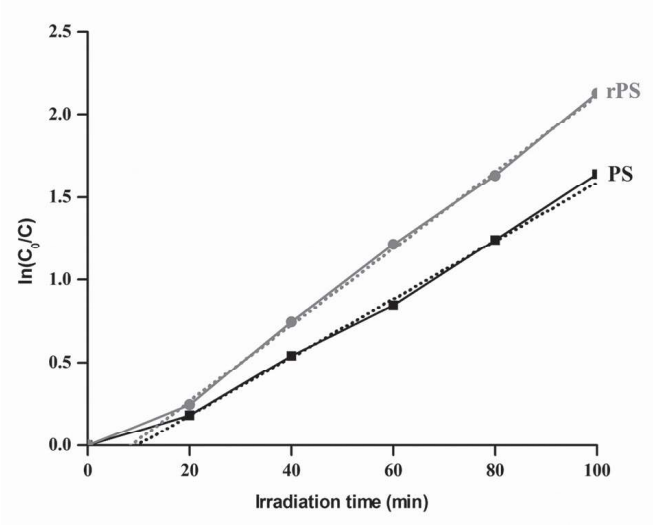

Fig.10 Kinetic plots of PS and rPS

Photocatalysts' photostability is important for practical application [39]. To assess the photostability of the rPS catalyst, recycle tests were performed for five cycles (Fig. 11 (a)). In the recovery process, a minimal reduction in degradation efficiency occurs after the fourth cycle due to the leaching of the catalyst surface, surface area loss, and aggregation [40]. Following the recycling test, XRD was obtained to confirm the rPS catalyst's reusable nature (Fig. 11(b)). No significant variation in the XRD pattern was observed, confirming its reusable nature. Photostabilization and anti-photocorrosion of the rPS catalyst are confirmed by this finding. Due to the rapid electron transfer and effective separation of charge carriers across the heterojunction, the rGO-PbS/SnO_2 exhibits high photoactivity and inhibits photocorrosion [41]. So, the rPS catalyst can be used to degrade *RhB* dye without producing secondary pollutants.

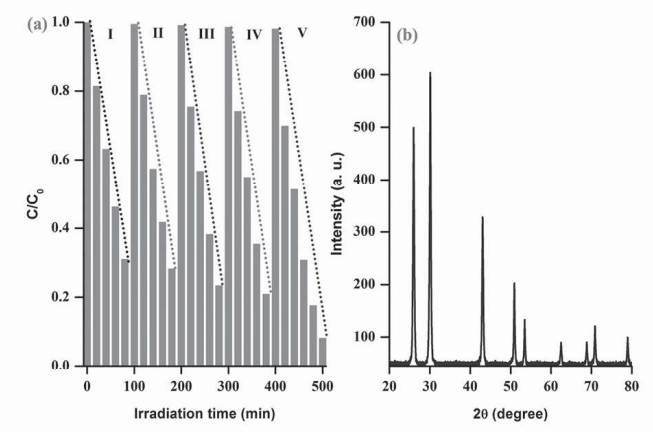

Fig.11 a) Recycle tests of rPS catalyst, b) Recycled rPS's XRD pattern

To study the mechanism of the degradation, E_{VB} and E_{CB} values of PbS and SnO_2 were found using the Eqns [42]:

$$E_{VB} = X - E^e + 0.5\,E_g \qquad (4)$$

$$E_{CB} = E_{VB} - E_g \qquad (5)$$

where X is the electronegativity, E^c is the energy of free electrons (4.5 eV). The E_{VB} and E_{CB} of PbS (E_g = 1.92 eV) were found to be 1.61 and -0.31 eV, and that of SnO_2 (E_g = 3.54 eV) were found to be 3.71 and 0.17 eV, respectively. When light falls on PS and rPS catalysts, valence electrons of both PbS and SnO_2 are excited and move toward their conduction bands, leaving holes in VB. Furthermore, with high

+ve VB edge potential, SnO_2 is more oxidative than PbS. Due to the negative CB potential of PbS, electrons diffuse from PbS to SnO_2. Due to SnO_2's positive VB potential, holes move from the VB of SnO_2 to PbS. Consequently, electrons and holes are effectively separated, and CB electrons of both PbS and SnO_2 react with oxygen to generate O_2^{*-} radicals. The VB holes of SnO_2 and PbS create OH^* radicals by OH^- (Fig. 12 (a)). In the case of the rPS catalyst, the electrons from the CB of PbS and SnO_2 move to rGO sheets, which can prolong the e^-/h^+ recombination rate, and the dye solution tested with the rPS catalyst contains a huge number of free carriers which generate more O_2^{*-} and OH^* radicals which convert the toxic dye molecules into CO_2/H_2O; thereby demineralizing them (Fig. 12 (b)).

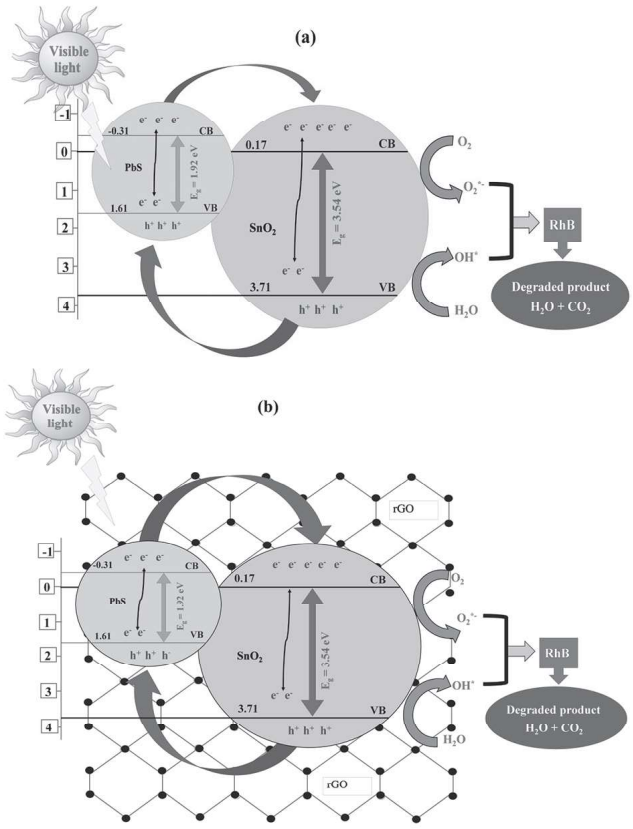

Fig.12 Photocatalytic mechanism involved with (a) PS and (b) rPS

3.7 *Antibacterial studies*

Figure 13 (a, b) depicts the antibacterial activities of PS and rPS, while Table 3 presents the zone of inhibition values.

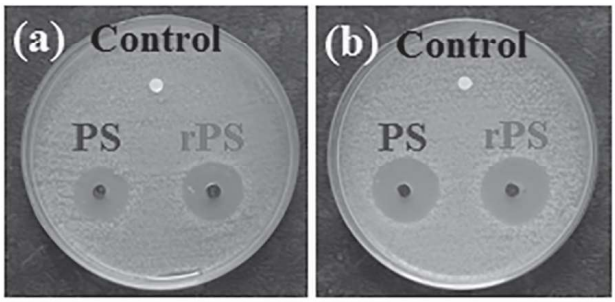

Fig.13 PS and rPS' bacterial suppression activity against a) *E. coli* and b) *S. aureus*

ZOI (mm)					
E. coli			***S. aureus***		
Control	**PS**	**rPS**	**Control**	**PS**	**rPS**
2	13	18	3	14	24

Table 3: ZOI values of control (Amkacin), PS and rPS

Both PS and rPS NCs exhibit better antibacterial activity than the control. PS and rPS NCs may exert antibacterial properties due to their internalization into the bacteria's cells via ion channels or proteins in the well of the cell, as well as reactive oxygen species (ROS) generation [31]. By oxidizing membrane lipids, ROS generation dysfunctions the cell wall and bacterial rupture [1]. As a general rule, ROS damages DNA, abasic sites, cell walls, and oxidized base lesions, breaks single and double strands, and oxidizes proteins and lipids, which alter cellular signal transduction pathways and lead to cell death [43]. By denaturing the proteins on the outer surface of the cell membrane, ROS, besides released metal ions, damages it by attracting the thiol groups [44]. The increased antibacterial efficiency realized for the rPS nanocomposite might be due to the following reasons: Upon coming into contact with the bacterial strains, the rGO wraps around the microbial membranes, allowing the hydrophilic moieties to form hydrogen bonds with the bacterial liposaccharides through delocalized conjugated π-π domains [45]. rGO-based NC can effectively resist bacterial strains by activating the mitochondrial pathway, which causes the mitochondria to lose their membrane potential and increases ROS generation [44]. ROS generation is also enhanced due to a reduced band gap. rGO's high specific surface

area promotes bacterial lipopolysaccharide adsorption to rPS NC via hydrogen bonding and Vander Waal's force, which releases more Pb^{2+} and Sn^{2+} ions, and the antibacterial activity of rPS NC was enhanced [46]. Compared to *E. coli* bacteria, both PS and rPS NCs showed effective resistance against *S. aureus* bacteria as it contain a thick peptidoglycan layer without an outer lipid membrane, which eases the entry of NPs inside the cell [47]. In gram -ve bacteria, the peptidoglycan layer is thin with an outer lipid membrane that restricts the entry of NPs, thereby reducing ROS production, and hence, bacterial growth inhibition nature is limited [48].

4. Conclusion

A single-pot synthesis approach was used to create rGO-PbS/SnO_2 (rPS) NC by reducing graphene oxide with *Psidium guajava* leaf extract. This composite was investigated and compared to PbS/SnO_2 (PS) NC synthesized via chemical precipitation for dye degradation and bacterial growth inhibition. The PS XRD pattern's cubic-shaped PbS and tetragonal-shaped SnO_2 peaks moved towards higher 2θ values upon the inclusion of rGO. rGO blending increased the crystallite size of PS from 29 to 34 nm. Pb-S and Sn-O related peaks observed in the FTIR spectra of both PS and rPS confirmed composite formation between them. Compared to PS, the rPS NC exhibited continuous absorbance in the visible region making it effective to utilize more visible light. After 100 minutes of light irradiation, the photodegradation effectiveness of PS against *RhB* dye rose from 82.5% to 93% with the addition of rGO. The bacterial growth inhibition zone value of PS improved with rGO blending. By wrapping microbial membranes and generating more ROS by inactivating the membrane potential of mitochondria, rGO makes PbS/SnO_2 nanocomposite to inhibit the growth of the tested pathogens. These outcomes clearly indicated that rGO blended PbS/SnO_2 nanocomposite could be an effective candidate for catalytic and biomedical applications.

Declaration of Conflict of Interest

No conflict of interest exists in the article.

Authors' contributions

"**Conceptualization** - A.R. Balu; **Methodology –** C. Rajashree; **Formal analysis and investigation –** M. Sriramraj; **Writing – original draft preparation –** N. Arunkumar; **Writing – review and editing –** A.R. Balu; **Funding acquisition –** K. Devendran; **Interpretation of data –** V. Rajamani, A. Vinith. All the authors read and approved the final manuscript."

Funding

The authors confirm that they received no grants, funds, or other forms of assistance in preparing this manuscript."

References

[1]. Suganya, M., Prabha, D., Anitha, S., Balamurugan, S., Nagarethinam, V. S., & Balu, A. R. (2017). Thermal behavior, magnetic and antimicrobial properties of PbS–CdO nanocomposite synthesized by a simple soft chemical route. *Journal of Materials Science: Materials in Electronics,* 28, 12348-12355.

[2]. Suganya, M., Balu, A. R., Prabha, D., Anitha, S., & Balamurugan, S. (2018). PbS–SnO_2 nanocomposite with enhanced magnetic, photocatalytic and antifungal properties. *Journal of Materials Science: Materials in Electronics,* 29, 1065-1074.

[3]. Chitra Devi, S., Sowmiya Devi, B., Balu, A. R., Devendran, K., Suganya, M., & Sriramraj, M. (2023). Improved Haacke's quality factor, third order nonlinear susceptibility and specific capacitance realized for PbS thin films through La^{3+} doping. *Ceramics International,* 49, 33793-33803.

[4]. Bouct, C., Laufer, D., Mahler, B., Nadal, B., Heuclin, H., Pedetti, S., Patriarche, G., & Dubertret, B. (2014). Synthesis of zinc and lead chalcogenide core and core/shell nanoplatelets using sequential cation exchange reactions. *Chemistry of Materials,* 26, 3002-3008.

[5]. Ferrari, S., Pampillo, L. G., & Saccone, F. D. (2016). Magnetic properties and environment sites in Fe doped SnO_2 nanoparticles. *Materials Chemistry and Physics,* 177, 206-212.

[6]. Vaezi, M. R., & Sadrnezhaad, S. K. (2007). Gas sensing behavior of nanostructured sensors based on tin oxide synthesized with different methods. *Materials Science and Engineering: B,* 140, 73-80.

[7]. Cui, X., Xu, W., Xie, Z., & Wang, Y. (2015). Hierarchical SnO_2@ SnS_2 counter electrodes for remarkable high-efficiency dye-sensitized solar cells. *Electrochimica Acta,* 180, 125-132.

[8]. Zheng, L. R., Zheng, Y. H., Chen, C. Q., Zhan, Y. Y., Lin, X. Y., Zhen, Q., Wei, K. M., & Zhu, J. F. (2009). Network Structured SnO_2/ZnO Heterojunction Nanocatalyst with High Photocatalytic Activity. *Inorganic Chemistry,* 48, 1819 - 1825.

[9]. Huang, X., Qi, X., Boey, F., & Zhang, H. (2012). Graphene-based composites. *Chemistry Society Reviews,* 41, 666-686.

[10]. Zhu, C., Guo, S., Fang, Y., & Dong, S. (2010). Reducing sugar: new functional molecules for the green synthesis of graphene nanosheets. *ACS Nano,* 4, 2429-2437.

[11]. Bose, D., & Chatterjee, S. (2016). Biogenic synthesis of silver nanoparticles using guava (*Psidium guajava*) leaf extract and its antibacterial activity against *Pseudomonas aeruginosa. Applied Nanoscience,* 6, 895-901.

[12]. Eda, G., Mattevi, C., Yamaguchi, H., Kim, H., & Chhowalla, M. (2009). Insulator to semimetal transition in graphene oxide. *The Journal of Physical Chemistry C*, 113, 15768-15771.

[13]. Yousaf, S., Zulfiqar, S., Din, M.I., Agboola, P. O., Aly Aboud, M. F., Warsi, M. F., Shakir, I. (2021). Solar light irradiated photocatalytic activity of ZnO-NiO/rGO nanocatalyst, *Journal of Materials Research and Technology*, 12, 999–1009 .

[14]. Zhao, Y., Li, Le., Zuo, Y., He, G., Chen, Q., Meng, Q., Chen, H. (2022). Reduced grapheme oxide supported ZnO/CdS heterojunction enhances photocatalytic removal efficiency of hexavalent chromium from aqueous solution, *Chemosphere*, 286, 131738.

[15]. Malik, A. R., Sharif, S., Shaheen, F., Khalid, M., Iqbal, Y., Faisal, A., Aziz, M. H., Atif, M., Ahmad, S., Fakhar-e-Alam, M., Hossain, N., Ahmad, H., Botmart, T. (2022). Green synthesis of RGO-ZnO mediated *Ocimum basilicum* leaves extract nanocomposite for antioxidant, antibacterial, antidiabetic and photocatalytic activity. *Journal of Saudi Chemical Society*, 26, 101438.

[16]. Chen Lin, Y., Tsai, D. C., Chang, Z. C., Shieu, F. S. (2018). Ultrasonic chemical synthesis of CdS-reduced grapheme nanocomposites with an enhanced visible light photoactivity. *Applied Surface Sci*ence, 440, 1227–1234 .

[17]. Rahimi, K., Zafarkish, H., Yazdani, A. (2018). Reduced grapheme oxide can activate the sunlight induced photocatalytic effect of NiO nanowires. *Materials and Design*, 144, 214–221.

[18]. El-Hout, S. I., El-Sheikh, S. M., Gaber, A., Shawky, A. (2020). Highly efficient sunlight-driven photocatalytic degradation of malachite green dye over reduced grapheme oxide supported CuS nanoparticles. *Journal of Alloys and Compounds*, 849, 156573.

[19]. Jyothilakshmi, V. P., Bhabhina, N. M., Dharsana, M. V., Sindhu, S. (2020). Wet chemical synthesis of lead sulphide nanoparticles and its application as light harvester in photovoltaice cell. Materials Today Proceedings, 33, 2125–2129.

[20]. Nallandran, R., Selvan, G., Balu, A. R. (2019). Photocatalytic performance of SnO_2 coupled with CdO nanoparticles against MY and RhB dyes. *Journal of Electronic Materials*, 48, 3676–3685.

[21]. Fu, X., Zhang, Y., Cao, P., Ma, H., Liu, P., Peng, J., Li, J., & Zhai, M. (2016). Radiation synthesis of CdS/reduced graphene oxide nanocomposites for visible-light-driven photocatalytic degradation of organic contaminant. *Radiation Physics and Chemistry,* 123, 79-86.

[22]. Jiang, L., Yao, M., Liu, B., Li, Q., Liu, R., Lv, H., Lv, S., Gong, C., Zou, B., Cui, T., & Liu, B. (2012). Controlled synthesis of CeO_2/graphene nanocomposites with highly enhanced optical and catalytic properties. *The Journal of Physical Chemistry C,* 116, 11741-11745.

[23]. Zhang, H., Lv, X., Li, Y., Wang, Y., & Li, J. (2010). P25-graphene composite as a high performance photocatalyst. *ACS Nano*, 4, 380-386.

[24]. Khan, Z., Chetia, T. R., Vardhaman, A. K., Barpuzary, D., Sastri, C. V., & Qureshi, M. (2012). Visible light assisted photocatalytic hydrogen generation and organic dye degradation by CdS - metal oxide hybrids in presence of graphene oxide. *RSC Advances,* 2, 12122-12128.

[25]. Peng, T., Li, K., Zhen, P., Zhiang, Q., & Zhang, X. (2012). Enhanced photocatalytic hydrogen production over graphene

oxide–cadmium sulfide nanocomposite under visible light irradiation. *The Journal of Physical Chemistry C,* 116, 22720-22726.

[26]. Suganya, M., Balu, A. R., Sowmiya Devi, B., Chitra Devi, S., Karthika, M., Kayathiri, C., Sriramraj, M., Devendran, K., Adityan, S. (2024). GO and rGO blended CdS nanoparticles for congo red dye deactivation, energy storage and growth inhibition aginst *Bacillus subtilis* and *Escherichia coli* bacterial strains: A comparative analysis. *Journal of Cluster Science*, 35, 827–843.

[27]. Suganya, M., Balu, A. R., Prabha, D., Anitha, S., & Balamurugan, S. (2018). Enhanced photocatalytic and antifungal properties of PbS nanopowder doped with Ag^{+} ions. *Journal of Materials Science: Materials in Electronics,* 29, 4312-4319.

[28]. Prabha, D., Ilangovan, S., Balamurugan, S., Suganya, M., Anitha, S., Nagarethinam, V. S., & Balu, A. R. (2017). Spectroscopic, magnetic and antibacterial properties of Sr-doped SnS_2nanopowders. *Optik,* 142, 301-310.

[29]. Zhang, H., He, Q., Wei, F., Ten, Y., Jiang ,Y., Zheng, G., Ding, G., & Jiao, Z. (2014). Ultrathin SnO nanosheets as anode materials for rechargeable lithium-ion batteries. *Materials Letters,* 120, 200-203.

[30]. Das, M. R., Sarma, R.K., Saika, R., Kale, V. S., Shelke, M. V., & Sengupta, P. (2011). Synthesis of silver nanoparticles in an aqueous suspension of graphene oxide sheets and its antimicrobial activity. *Colloids and Surfaces B: Biointerfaces,* 83, 16-22.

[31]. Manjula, N., & Balu, A. R. (2017). Double doping (Mn+ Cl) effects on the structural, morphological, photoluminescence, optoelectronic properties and antibacterial activity of CdO thin films. *Optik*, 130, 464-472.

[32]. Sowribabu, K., Ramachandra reddy, A., Sujitha, Ch., & Venugopal Reddy, K. (2013). Optimization of UV emission intensity of ZnO nanoparticles by changing the excitation wavelength. *Materials Letters,* 99, 97-100.

[33]. Ravishankar, S., Balu, A. R., Usharani, K., Balamurugan, S., Prabha, D., & Nagarethinam, V. S. (2017). Optical and magnetic properties of PbS thin films doped with Fe^{2+} ions. *Optik* ,134, 121-127.

[34]. Gu, F., Wang, S. F., Lu, M. K., Zhou, G. J., Xu, D., & Yuan, D. R. (2004). Photoluminescence Properties of SnO_2 Nanoparticles Synthesized by Sol−Gel Method. *The Journal of Physical Chemitry B,* 108, 8119-8123.

[35]. Prabha, D., Ilangovan, S., Suganya, M., Anitha, S., Balamurugan, S., & Balu, A. R. (2017). TG-DSC analysis, magnetic and antifungal properties of Al-doped SnS_2 nanopowders. *Journal of Materials Science: Materials in Electronics,* 28, 15556-15564.

[36]. Sivaraman, T., Nagarethinam, V. S., & Balu, A. R. (2016). Properties of CdS films doped with magnesium and fluorine. *Surface Engineering,* 32, 596-600.

[37]. Irshad, A., Farooq, F., Warsi, M. F., Shaheen, N., Elnaggar, A.Y., Hussein, E. E., El-Bahy, Z. M., & Shahid M. (2022). Ag-doped $FeCo_2O_4$ nanoparticles and their composite with flat 2D reduced graphene oxide sheets for photocatalytic degradation of colored and colorless compounds. *Flatchem*, 31, 100325.

[38]. Kumar, S., Kaushik, R.D., & Purohit, L.P. (2023). RGO supported ZnO/SnO_2 Z-scheme heterojunctions with enriched ROS production towards enhanced photocatalytic mineralization of phenolic compounds and antibiotics at low temperature. *Journal of Colloid and Interface Science,* 632, 196-215.

[39]. Xu, D., Cheng, B., Cao, S., & Yu, J. (2015). Enhanced photocatalytic activity and stability of Z-scheme Ag_2CrO_4-GO composite photocatalysts for organic pollutant degradation. *Applied Catalyis B: Environmental,* 164, 380-388.

[40]. Yousaf, S., Zulfiqar, S., Din, M. I., Agboola, P. O., Aly Aboud, M. F., Warsi, M.F., & Shakir, I. (2021). Solar light irradiated photocatalytic activity of ZnO–NiO/rGOnanocatalyst. *Journal of Material Research and Technology,* 12, 999-1009.

[41]. Feng, C., Deng, Y., Tang, L., Zeng, G., Wang, J., Yu, J., Liu, Y., Peng, B., Feng, H., & Wang, J. (2018). Core-shell Ag_2CrO_4/N-GQDs@g-C_3N_4 composites with anti-photocorrosion performance for enhanced full-spectrum-light photocatalytic activities. *Applied Catalysis B: Environmental,* 239, 525-536.

[42]. Ahmad, N., Sultana, S., Sabir, S., & Khan, M. Z. (2020). Exploring the visible light driven photocatalysis by reduced graphene oxide supported Ppy/CdS nanocomposites for the degradation of organic pollutants. *Journal of Photochemistry and Photobiology A: Chemstry,* 386,112129.

[43]. Diakowska, D., Lewandowski, A., Kopee, W., Diakowski, W., & Chrzanowska, T. (2007). Oxidative DNA damage and total antioxidant status in serum of patients with esophageal squamous cell carcinoma. *Journal of Hepato-Gastroenterology,* 78, 1701-1704.

[44]. Ceril Jeoffrey, A., Jothi Ramalingam, S., Murugaiah, K., & Balu, A. R. (2023). Highly photoactive rGO-MnO_2/CuO nanocomposite photocatalyst for the removal of metanil yellow dye and bacterial resistance against Pseudomonas Aeruginosa. *Chemical Physics Impact,* 6,100246.

[45]. Dat, N. M., Thinh, D. B., Huong, L. M., Tinh, N. T., Linh, N. T. T., Hai, N. D., Vict, N. D., Dat, N. T., Phong, M. T., & Hieu, N. H. (2022). Facile synthesis and antibacterial activity of silver nanoparticles-modified graphene oxide hybrid material: the assessment, utilization, and anti-virus potentiality. *Mater ials Today Chemistry,* 23,100738.

[46]. Gu, D., Cheng, X., Zhei, X., Sun, S., Li, Z., Liu, T., Dong, L., & Yin, Y. (2016). Efficient synthesis of silver-reduced graphene oxide composites with prolonged antibacterial effects. *Ceramics International,* 42, 9769-9778.

[47]. Reddy, N. J., Nagoor Vali, D., Rani, M., & Rani, S. S. (2014). Evaluation of antioxidant, antibacterial and cytotoxic effects of green synthesized silver nanoparticles by Piper longum fruit. *Materials Science and Engineering: C,* 34, 115-122.

[48]. Ganesh, M., Lee, S. G., Jayaprakash, J., Mohankumar, M., & Jang, H. T. (2019). HydnocarpusalpinaWt extract mediated green synthesis of ZnO nanoparticle and screening of its anti-microbial, free radical scavenging, and photocatalytic activity. *Biocatalysis and Agricultural Biotechnology,* 19,101129.